

1-2022

## Freshwater Transport in the Scotian Shelf and Its Impacts on the Gulf of Maine Salinity

Z. Wang

*Virginia Institute of Marine Science*

D. Li

H. Xue

A. C. Thomas

Yinglong J. Zhang

*Virginia Institute of Marine Science*

*See next page for additional authors*

Follow this and additional works at: <https://scholarworks.wm.edu/vimsarticles>



Part of the [Oceanography Commons](#)

---

### Recommended Citation

Wang, Z.; Li, D.; Xue, H.; Thomas, A. C.; Zhang, Yinglong J.; and Chai, F., Freshwater Transport in the Scotian Shelf and Its Impacts on the Gulf of Maine Salinity (2022). *Journal of Geophysical Research: Oceans*, 127(1), e2021JC017663.  
doi: 10.1029/2021JC017663

This Article is brought to you for free and open access by the Virginia Institute of Marine Science at W&M ScholarWorks. It has been accepted for inclusion in VIMS Articles by an authorized administrator of W&M ScholarWorks. For more information, please contact [scholarworks@wm.edu](mailto:scholarworks@wm.edu).

---

**Authors**

Z. Wang, D. Li, H. Xue, A. C. Thomas, Yinglong J. Zhang, and F. Chai

## Freshwater Transport in the Scotian Shelf and Its Impacts on the Gulf of Maine Salinity

Zhengui Wang<sup>1,2</sup> , Denghui Li<sup>1</sup> , Huijie Xue<sup>1</sup> , Andrew C. Thomas<sup>1</sup>, Yinglong J. Zhang<sup>2</sup> , and Fei Chai<sup>1</sup> 

<sup>1</sup>School of Marine Sciences, University of Maine, Orono, ME, USA, <sup>2</sup>Virginia Institute of Marine Science, College of William & Mary, Gloucester Point, VA, USA

### Key Points:

- NorthEast Shelf Seas model was constructed and validated to study freshwater transport (FWT) in the Scotian Shelf (SS)
- Southwestward wind can significantly increase the FWT in the SS
- Anticyclonic eddies blocked the FWT in the SS resulting in higher Gulf of Maine salinity in 2018

### Supporting Information:

Supporting Information may be found in the online version of this article.

### Correspondence to:

H. Xue,  
[hxue@maine.edu](mailto:hxue@maine.edu)

### Citation:

Wang, Z., Li, D., Xue, H., Thomas, A. C., Zhang, Y. J., & Chai, F. (2022). Freshwater transport in the Scotian Shelf and its impacts on the Gulf of Maine salinity. *Journal of Geophysical Research: Oceans*, 127, e2021JC017663. <https://doi.org/10.1029/2021JC017663>

Received 14 JUN 2021  
Accepted 7 JAN 2022

### Author Contributions:

**Conceptualization:** Zhengui Wang, Huijie Xue, Fei Chai  
**Data curation:** Zhengui Wang  
**Formal analysis:** Zhengui Wang, Denghui Li, Huijie Xue, Fei Chai  
**Funding acquisition:** Huijie Xue, Fei Chai  
**Investigation:** Zhengui Wang, Huijie Xue  
**Methodology:** Zhengui Wang, Denghui Li, Huijie Xue, Andrew C. Thomas, Yinglong J. Zhang  
**Project Administration:** Huijie Xue, Fei Chai  
**Resources:** Zhengui Wang, Denghui Li, Huijie Xue  
**Software:** Zhengui Wang  
**Supervision:** Huijie Xue  
**Validation:** Zhengui Wang, Huijie Xue  
**Visualization:** Zhengui Wang  
**Writing – original draft:** Zhengui Wang  
**Writing – review & editing:** Zhengui Wang, Denghui Li, Huijie Xue, Andrew C. Thomas, Yinglong J. Zhang, Fei Chai

**Abstract** A 3D unstructured-grid ocean circulation model covering the continental shelf and coastal seas around New England is used to investigate freshwater transport (FWT) on the Scotian Shelf (SS) and its impact on the salinity in the Gulf of Maine (GoME). The model was first validated using observed elevation, velocity, temperature, and salinity at multiple locations, demonstrating generally high model skills. Intraseasonal variabilities of freshwater fluxes in 2017 and 2018 were then analyzed across different transects around SS and Browns Bank (BB). These indicated that the flow pattern in SS during 2017 was consistent with previous understanding: low salinity water flows southwestward along the shelf and turns into the GoME around BB. However, in 2018, most of the low salinity water did not enter the GoME, but was transported to the open ocean. The most striking difference occurred early in the year when the FWT, normally at its maximum, was practically stopped by an anticyclonic eddy impinging upon the shelf break near the western end of SS. Then in March, in contrast to the prevailing eastward wind, two southwestward wind events occurred that induced an excessive amount of FWT in SS. We further showed that when anticyclonic eddies impinge on the shelf break, the typical geostrophic balance associated with southwestward flow is interrupted, and a new geostrophic balance is established with the directions of pressure gradient force and flow reversed. The influence from anticyclonic eddies explains the abnormally low FWT in SS and higher GoME salinity in 2018.

**Plain Language Summary** In this research, we built an ocean circulation model around New England area and verified the model performance in capturing the variations of water level, velocity, temperature, and salinity. We used this model to analyze the movement of freshwater content that is contained in the seawater on the Scotian Shelf (SS) in 2017–2018, and studied its influence on the salinity in the downstream Gulf of Maine (GoME). The model shows that in 2017 the freshwater flew southwestward along the SS and then entered into the GoME, while in 2018 most of the freshwater did not enter the GoME, but went to the open ocean. The absence of freshwater input from the SS was caused by frequent anticyclonic eddies around the SS, which resulted in higher salinity in the GoME. In addition, we found that the southwestward wind can significantly increase the freshwater flow on the SS.

## 1. Introduction

One general feature along the New England coast and continental shelf is that cold water on the Scotian Shelf (SS) moves southwestward, passing the Gulf of Maine (GoME) region before making its way to the downstream Mid-Atlantic Bight (Bisagni et al., 1996; Townsend et al., 2015). The GoME is a broad shallow sea along the US northeast coast extending from Cape Cod, US to Cape Sable, Canada. It is an important fishing ground due to its high biological productivity, especially around Georges Bank where the annual primary production can exceed  $400 \text{ g[C]}\cdot\text{m}^{-2} \text{ yr}^{-1}$  (Incze et al., 2010; Moriarty et al., 2016; Reilly et al., 1987). As an important driver for the GoME, the spatiotemporal variability of the upstream SS water is the focus of this study. Aspects of SS water impacts on GoME hydrodynamics will be further explored in a companion article (Li et al., 2021).

The GoME is a strong tidally impacted region dominated by the semidiurnal M2 constituent (Greenberg, 1979; Xue et al., 2000). It is characterized by heterogeneous bathymetry and three separate deep basins (Georges, Jordan, and Wilkinson) that have depths larger than 200 m (Townsend et al., 2006). The GoME is semi-enclosed, and its exchange with the open Atlantic Ocean is largely restricted by Georges Bank and Browns Bank (BB). Slope water inflow to the GoME is through the narrow Northeast Channel between these two banks (Ramp et al., 1985), while the shallower Great South Channel located to the west of Georges Bank is a major exit of waters in the

upper 50 m (Xue et al., 2000). The Northeast Channel directly connects to the deepest reservoir in the GoME, Georges Basin, where the saline slope water inflow is first deposited, and then spreads further into Jordan and Wilkinson basins. Along the transport pathway of this Maine Bottom Water, its properties get eroded by the Maine Intermediate Water through mixing processes (Brown & Irish, 1993).

Another major exchange of GoME water with the Atlantic Ocean is through the SS where water enters the gulf around Cape Sable and joins the GoME circulation (Smith et al., 2001). This Scotian Shelf Water (SSW) has low salinity and temperature (32.0 PSU, 2°C) compared to the slope waters (34.6 PSU, 6°C) mentioned above (Townsend et al., 2015). Following the mean cyclonic circulation pattern in the GoME, this cold and fresh water mass from SS travels northward until reaching the mouth of the Bay of Fundy where it branches toward the coast of Maine and becomes part of the Eastern Maine Coast Current (Pettigrew et al., 2005, 1998). SSW is a significant freshwater source to the GoME, accounting for more than half of the freshwater budget in the GoME (Bigelow, 1927; Smith, 1983). There appeared to be a significant increase of SSW during the mid-1990s that was accompanied by a decrease of slope water inflow (Li et al., 2014; Smith et al., 2001, 2012). Feng et al. (2016) further estimated the freshwater flux associated with SSW and demonstrated its correlation with the salinity at 50-m depth along the coast of Maine. SSW may also play an important role in the heat budget for the GoME (Bigelow, 1927; Townsend et al., 2015). Shore et al. (2000) identified the pathway of SSW that provides nutrients and organisms to the GoME by using particle tracking methods. Although concentrations are low, nutrients in SSW can fuel the spring bloom in SS and the eastern GoME as increased buoyancy allows phytoplankton in the euphotic zone to readily uptake nutrients (Ji et al., 2007). In contrast, nutrients contained in the Maine Bottom Water must be mixed upwards to the surface layer before they can be utilized (Drinkwater et al., 1998; Townsend et al., 2006). In addition, SSW can impact the temperature and salinity on Georges Bank by directly crossing over the Northeast Channel (Bisagni et al., 1996; Cho et al., 2002; Smith et al., 2001).

Given the importance of SSW to the GoME, investigations of variations of SSW under different forcing conditions and corresponding mechanisms are important. This direction of research not only illustrates the details of SSW transport on the SS, but also helps to explain downstream variations in the GoME. The main feature of the circulation on SS is the southwestward flow that carries fresher and colder water into the downstream regions of GoME and Georges Bank. This is most prominent in winter and spring (Han et al., 1997; Ji et al., 2008; Loder, 1998; Loder et al., 2003). Li et al. (2014) proposed a “valve” mechanism where the strength of northeastward wind modulates the along-shelf transport by affecting the geostrophic balance in the cross-shelf direction. When the northeastward wind is strong, the along-shelf flow becomes weak in the SS (the tightened valve) as the water level lowers near the coast and the surface elevation slants from the southeast to the northwest. When the northeastward wind relaxes, the along-shelf flow becomes stronger (an open valve), the water level rises along the coast, and the surface elevation slants slightly from the northwest to the southeast. On smaller scales, the complex bathymetry characterized by many shallow banks, deep basins, and trenches in SS induces localized meanders and eddies (Drinkwater et al., 2002; Hannah et al., 2001).

The lack of time series measurements on SS poses limits on our ability to further analyze the SSW inflow and its variability at shorter timescales. For example, intraseasonal variations of SSW inflow are still not well understood, as well as the associated freshwater input to the GoME. Also, there is a need to further investigate factors that control the SSW to better understand its transport in the SS. The advancement of numerical modeling in recent years provides an alternative approach to explore this region with better spatiotemporal resolutions. In this study, we constructed a numerical model for the continental shelf and coastal seas around the New England region, referred as NorthEast Shelf Seas (NESS) model hereafter, to study the SSW as well as other factors impacting the GoME. The focus is on the freshwater flux associated with SSW in two contrasting years of 2017–2018. In the following, we first describe the NESS model and our method in Section 2. Then we present model validation in Section 3, followed by results and analyses of dynamical processes in Sections 4 and 5, and a summary in Section 6.

## 2. Method

### 2.1. The NESS Model

The numerical model we adopted is Semi-implicit Cross-scale Hydroscience Integrated System Model (SCHISM; Zhang et al., 2016). SCHISM offers the Generic Length-Scale model of Umlauf and Burchard (2003) for the

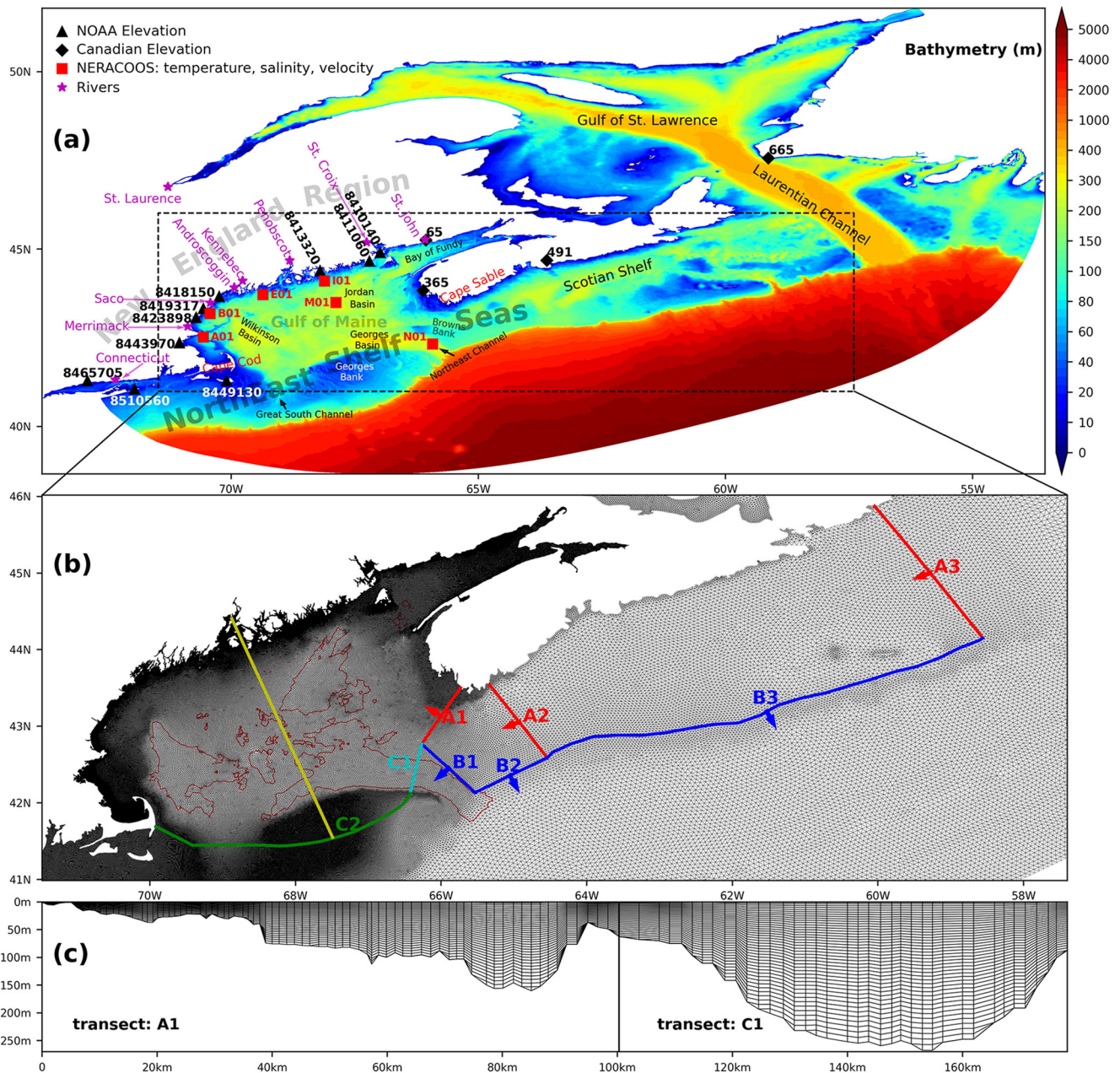


**Figure 1.** (a) NESS model domain with bathymetry in color. Black triangles mark the NOAA tidal gauge stations; black diamonds mark the Canadian tidal gauge stations; and red squares mark the NERACOOS mooring stations. (b). Model grid covering the GoME and SS study area. The GoME region is enclosed by transects A1 and C1-2, and the division between the western GoME and the eastern GoME is shown by the yellow line. The thin red lines in GoME are 200 m isobaths. The region around Browns Bank is enclosed by transects A1-2 and B1-2, and the SS is enclosed by transects A2-3 and B3. Freshwater fluxes are computed across these transects. The arrow on each transect defines the positive direction of fluxes. (c). Vertical grid along transects A1 and C1.

vertical viscosity and diffusivity, and a standard Laplacian formulation for the horizontal diffusion. For more details on SCHISM model, please refer to the SCHISM manual ([http://ccrm.vims.edu/schismweb/schism\\_manual.html](http://ccrm.vims.edu/schismweb/schism_manual.html)).

### 2.1.1. Bathymetry and Model Grid

Figure 1a shows the NESS model domain with bathymetry in the background. It extends from the deep ocean where the depth exceeds 5,000 m to the US and Canadian coasts and includes the entire GoME and Gulf of St. Lawrence along with the lower reaches of the St. Lawrence River. The bathymetry data come from two sources.

US Coastal Relief Model (USCRM) data (<https://www.ngdc.noaa.gov/mgg/coastal/crm.html>) with a resolution of 3 arc-seconds are used for the US coastal ocean wherever possible. For the areas where USCRM is not available, bathymetry data from the General Bathymetric Chart of the Oceans (GEBCO) with a resolution of 30 arc-seconds (<https://www.gebco.net/>) are used. The main features along the continental shelf in Figure 1a are two incisions that play crucial roles in the water exchange between the ocean and shelf. In the eastern part of the continental shelf, the large Laurentian Channel cuts into the Gulf of St. Lawrence. In the middle part, a relatively smaller Northeast Channel cuts into the GoME. Figure 1a also shows the locations of time series stations including 10 NOAA tidal gauge stations (<https://tidesandcurrents.noaa.gov/>), four Canadian water level stations (<http://www.isdm-gdsi.gc.ca/isdm-gdsi/twl-mne/index-eng.htm>), and six NERACOOS buoy stations.

Figure 1b shows the model grid around the GoME and SS. SCHISM provides flexibilities in model grid generation to resolve regions of interest with fewer constraints than traditional structured grid models allowing it to more faithfully represent the geomorphological features. In the GoME, the resolution is  $\sim 200$  m nearshore. As water depth increases, the grid size gradually increases to around 1 km at  $\sim 100$  m water depths. Apart from the GoME, grid resolution in the continental shelf is generally larger than 1 km, and it is  $\sim 6$  km near the ocean boundary. In the vertical, localized sigma coordinate system (LSC<sup>2</sup>) with shaved bottom cells (Zhang et al., 2015) is used to better represent the bathymetric features without the need for bathymetry smoothing. Figure 1c shows an example of a vertical grid along transects A1 and C1. Transect A1 has a rugged bottom and the water depth changes rapidly from coast to offshore, while transect C1 has a relatively smooth bathymetry with large depths across the Northeast Channel. Note that the tilt of grid cells is greatly exaggerated in Figure 1c because, in reality, the horizontal length of grid cells is much larger than their thickness.

## 2.2. Model Configuration

NESS model is configured with two open boundaries. The major one is in the deep ocean off the continental slope and the minor one is located in the northeastern Gulf of St. Lawrence. For subtidal variations, the boundary condition of the NESS model is extracted from the HYCOM reanalysis (model versions: GLBu0.08 and GLBv0.08) including elevation, current, temperature and salinity (<https://www.hycom.org/>). For tidal forcing, elevation and current of eight constituents (O1, K1, Q1, P1, M2, S2, K2, N2) are derived from the FES2014 tide database (<https://datastore.cls.fr/catalogues/fes2014-tide-model/>). The sum of the tidal and sub-tidal elevation and current (the summation is done inside SCHISM) together with the HYCOM temperature and salinity are applied along the open boundaries to force the NESS model. The initial conditions of temperature and salinity are interpolated from HYCOM model, while the initial values of velocity ( $u$ ,  $v$ ) and elevation are set to zero. Atmospheric forcing for the NESS model is from the North American Regional Reanalysis, including wind, air temperature, pressure, solar radiation, and precipitation ([www.emc.ncep.noaa.gov/mmb/rreanl](http://www.emc.ncep.noaa.gov/mmb/rreanl)). River flow provides important sources of buoyancy to the GoME and plays an important role along the Eastern and Western Maine Coastal Currents (Pettigrew et al., 2005). To better represent the river influence in our model, we include all the major rivers (St. John, Penobscot, Kennebec-Androscoggin, Merrimack), as well as many smaller rivers (e.g., Saco River) around the GoME (see Figure 1a). Flow rates are from USGS (<https://waterdata.usgs.gov/nwis/rt>). When USGS data are missing, we correlate the flow rate to nearby available USGS flow data by using watershed areas. In addition, the St. Lawrence River, which has a large discharge with an annual mean flow rate of over  $1.4 \times 10^4$  m<sup>3</sup>/s, is also considered in the model. Canadian hydrological flow rate data at the upstream Montreal station (02OA016) is used to estimate the St. Lawrence River discharge based on its correlation with flow data at downstream station (02OJ032; [https://wateroffice.ec.gc.ca/index\\_e.html](https://wateroffice.ec.gc.ca/index_e.html)).

The model was run from 2014 to 2018 with a time step of 120 s. The model results are validated against observations including elevation, temperature, salinity, and velocity. In this study, only the results in two years (2017 and 2018) with contrasting conditions in the SS are analyzed, and our companion article (Li et al., 2021) analyzed the results in other years.

## 2.3. Computation of Freshwater Flux

In this study, we focus on the SSW by studying the associated freshwater transport (FWT), particularly the freshwater flux through the different transects shown in Figure 1b. We follow the definition of freshwater index:

$$F = (S_0 - S)/S_0 \quad (1)$$

from Brown and Irish (1993) to represent the freshwater contained in saline water, where  $S$  is the salinity and  $S_0$  (35.4 PSU) is a reference salinity value, chosen to represent the slope water with Gulf Stream origin. We limit the value of freshwater index within the range of 0, 1, which means that the freshwater content is regarded as zero when salinity is higher than  $S_0$ . By integrating the freshwater index in the vertical, we get the distribution of equivalent freshwater thickness as the following:

$$h^F(x, y) = \int_{-H}^{\eta} F(x, y) \cdot dz. \quad (2)$$

In order to describe the distribution of FWT in space, freshwater velocity is defined as the following:

$$\vec{U}^F = F \cdot \vec{U}, \quad (3)$$

where  $\vec{U}$  is water velocity. We then adopt the method implemented by Feng et al. (2016) and Smith et al. (2001) to compute the freshwater flux as the following:

$$Q^F = \int_0^L dl \int_{-H}^{\eta} dz \cdot \vec{U}_{\perp}^F, \quad (4)$$

where  $\eta$  is the surface elevation,  $H$  the water depth,  $L$  the length of transect, and  $\vec{U}_{\perp}^F$  the freshwater velocity component that is perpendicular to the transect. The sign of  $Q^F$  comes from  $\vec{U}_{\perp}^F$ , and positive directions are shown by the short arrows associated with each transect in Figure 1b.

### 3. Model Validation

#### 3.1. Tidal Elevation and Velocity

The modeled and observed semi-diurnal and diurnal tidal amplitudes and phases at 10 NOAA stations and 4 Canadian stations are compared (Figure S1 in Supporting Information S1) with the differences given in Table 1. Both amplitudes and phases from the model match the observations well across all stations for semi-diurnal tides. The predominant tidal component is the semi-diurnal M2 tide, and larger M2 errors appear at stations 8410140, 65, and 365 with error values exceeding 15 cm (Table 1), and the corresponding phase differences are larger than 15°. The cause for larger errors may be due to two factors: lack of high-resolution bathymetry data, and larger absolute tidal amplitudes (see Figure S1 in Supporting Information S1; note the relative errors are still  $\leq 10\%$ ). Except for these three stations, most of the amplitude errors at other stations are smaller than 5 cm; most of the phase differences are less than 15° for M2, S2, and K2, and less than 20° for N2. Diurnal tides have much smaller amplitudes than semi-diurnal tides (Figure S1 in Supporting Information S1). The largest diurnal tide is K1 with amplitudes around 10 cm. Table 1 shows that the model systematically underestimates the amplitudes of all diurnal tides. The absolute errors of diurnal tidal amplitudes are generally smaller than 3 cm with the largest value of 3.6 cm at station 8410140 for K1 tide.

Figure 2 shows the comparison of M2 tidal velocities at six NERACOOS stations and multiple depths for both amplitude and phase. Additional comparisons of tidal residual velocities as well as comparisons to shipboard Acoustic Doppler Current Meter data were provided in the companion article (Li et al., 2021). For the three stations (A01, B01, and E01) located in the western GoME, the modeled velocity profiles of M2 tide compare well with observational data. Both the model and observation show that at station A01,  $U$  velocity dominates over  $V$  velocity; at station B01,  $U$  velocity is comparable to  $V$  velocity; while at station E01,  $V$  velocity dominates over  $U$  velocity. For these three stations, the root mean squared error (RMSE) of  $U$  velocity ranges from 0.8 cm/s at E01 to 1.5 cm/s at A01, while the RMSE of  $V$  velocity ranges from 1.0 cm/s at A01 and B01 to 1.6 cm/s at E01.

I01 is a coastal station in the eastern GoME, M01 is located in Jordan Basin, while N01 is located on the eastern side of Northeast Channel. For these three stations, the NESS model reproduces the general patterns of M2 velocity profiles, but with relatively larger errors compared to the three stations in the western GoME. At I01 and

**Table 1**  
*Differences in Amplitude and Phase of Tidal Elevation Between Model and Observation*

Tidal elevation		O1	K1	Q1	P1	M2	S2	K2	N2
Amplitude (cm)	8465705	-0.4 (7.7%)	-0.3 (3.6%)	-0.3 (25.3%)	0.2 (8.4%)	-6.5 (7.2%)	0.9 (6.2%)	0.5 (18.2%)	-0.1 (0.5%)
	8510560	-0.3 (8.0%)	0.1 (1.7%)	-0.3 (24.9%)	-0.1 (3.9%)	1.8 (5.9%)	0.3 (5.3%)	0.3 (23.8%)	0.1 (1.9%)
	8449130	-1.4 (18.9%)	-1.1 (13.1%)	-0.2 (17.7%)	-0.5 (16.1%)	-4.3 (9.5%)	-0.1 (3.1%)	0.0 (2.7%)	1.6 (14.0%)
	8443970	-1.9 (20.5%)	-2.4 (19.5%)	-0.2 (11.5%)	-0.9 (20.9%)	-3.1 (2.2%)	1.5 (7.2%)	1.0 (22.4%)	4.5 (14.6%)
	8423898	-1.8 (19.8%)	-2.4 (19.6%)	-0.3 (16.8%)	-1.0 (21.5%)	0.3 (0.2%)	2.4 (12.3%)	1.0 (25.2%)	5.4 (18.6%)
	8419317	-2.0 (21.6%)	-2.7 (21.2%)	-0.2 (13.3%)	-1.1 (23.2%)	-2.5 (1.8%)	1.8 (9.2%)	0.9 (22.6%)	4.4 (14.7%)
	8418150	-2.1 (21.9%)	-3.1 (23.5%)	-0.2 (11.8%)	-1.4 (28.2%)	-3.0 (2.1%)	1.9 (9.1%)	1.0 (21.7%)	4.5 (14.4%)
	8413320	-2.1 (22.3%)	-3.1 (23.9%)	-0.4 (23.6%)	-1.3 (26.2%)	-0.8 (0.5%)	3.1 (13.1%)	1.2 (23.1%)	5.8 (16.6%)
	8411060	-2.0 (20.7%)	-3.0 (22.7%)	-0.2 (14.7%)	-1.1 (22.7%)	0.8 (0.4%)	4.4 (14.2%)	1.8 (27.6%)	8.1 (18.8%)
	8410140	-2.4 (24.1%)	-3.6 (26.1%)	-0.4 (23.0%)	-1.7 (33.1%)	-15.5 (5.6%)	-0.8 (1.9%)	0.9 (10.7%)	2.4 (4.4%)
	65	-1.7 (17.2%)	-2.8 (20.0%)	0.0 (3.0%)	-1.0 (19.7%)	15.0 (4.7%)	9.9 (20.7%)	4.7 (50.3%)	15.3 (24.0%)
	365	-1.5 (17.3%)	-2.8 (22.1%)	-0.2 (10.8%)	-1.0 (22.8%)	17.8 (10.4%)	5.8 (21.9%)	2.1 (38.1%)	9.9 (27.7%)
	491	-0.3 (6.6%)	-2.3 (25.4%)	0.3 (75.8%)	-0.9 (27.3%)	-0.2 (0.3%)	0.2 (1.6%)	0.3 (11.2%)	0.0 (0.1%)
	665	-2.0 (27.7%)	-1.6 (23.1%)	-0.2 (22.2%)	-0.6 (22.5%)	2.7 (6.1%)	-0.6 (4.5%)	0.0 (1.6%)	0.6 (6.3%)
	Mean	-1.6 (18.2%)	-2.2 (19.0%)	-0.2 (21.0%)	-0.9 (21.2%)	0.2 (4.1%)	2.2 (9.3%)	1.1 (21.4%)	4.5 (12.6%)
	Phase (degree)	8465705	2.1	-3.4	8.9	-7.2	8	-1.9	-7.6
8510560		5.1	-4.1	17.8	-10.3	-1.7	-4.8	-2.1	6.8
8449130		9.2	-16.9	18.9	-19.7	1.6	-0.9	-11.9	11.1
8443970		17	-4.9	25.4	-5.1	12.5	4.9	7.3	18.6
8423898		19.3	-7.8	31.6	-6.4	9.4	2.5	-3.9	16.1
8419317		18.2	-7.9	26.9	-7.4	9.2	1.3	-3.2	15.2
8418150		20.9	-6.7	30.7	-6.5	12	4.1	-0.7	18.7
8413320		24.4	-8.6	37.9	-4	13.4	6.6	-4.9	19.4
8411060		20.4	-6	32.4	-7.8	15.1	6.4	1	19.3
8410140		35.7	6.7	51.7	7	31.5	26.3	22.7	39.3
65		19.7	-3.9	32.4	-8.1	18.5	8.8	9	21.2
365		21.6	-6	27.6	-5.3	16.6	8.6	6.2	21
491		56.8	18.3	58.8	17.3	10.8	-0.7	-4.8	14.7
665		0.1	-21.2	23.3	-17.2	22.2	15.2	14.2	27
Mean		19.3	-5.2	30.3	-5.8	12.8	5.5	1.5	18.6

*Note.* The errors are listed for four semi-diurnal tides and four diurnal tides at NOAA and Canadian tidal gauge stations. Numbers in brackets indicate the relative difference of tidal amplitude.

M01, the  $V$  velocities dominate over the  $U$  velocities, while at N01, the  $U$  velocity dominates. In addition, the magnitude of tidal velocity at N01 is significantly larger than those at the other stations. The RMSE of  $U$  velocity is 3.8, 1.9, and 9.0 cm/s for I01, M01, and N01, respectively; while the corresponding RMSE of  $V$  velocity is 3.4, 4.6, and 7.7 cm/s, respectively. The phase comparison of M2 tidal velocity in the model matches the measurements very well for both  $U$  and  $V$  components at different depths across all stations.

### 3.2. Temperature and Salinity

Figure 3a compares modeled temperature and salinity with those at six NERACOOS stations. For the three stations in the western GoME (A01, B01, E01), the surface (1 m) temperature varies from 10.0°C to 11.4°C and the surface salinity from 31.6 PSU to 32.1 PSU, while at 50 m the temperature varies from 6.2°C to 7.9°C and the salinity from 32.4 PSU to 32.6 PSU. In general, the model captures the vertical distributions although discrepancies

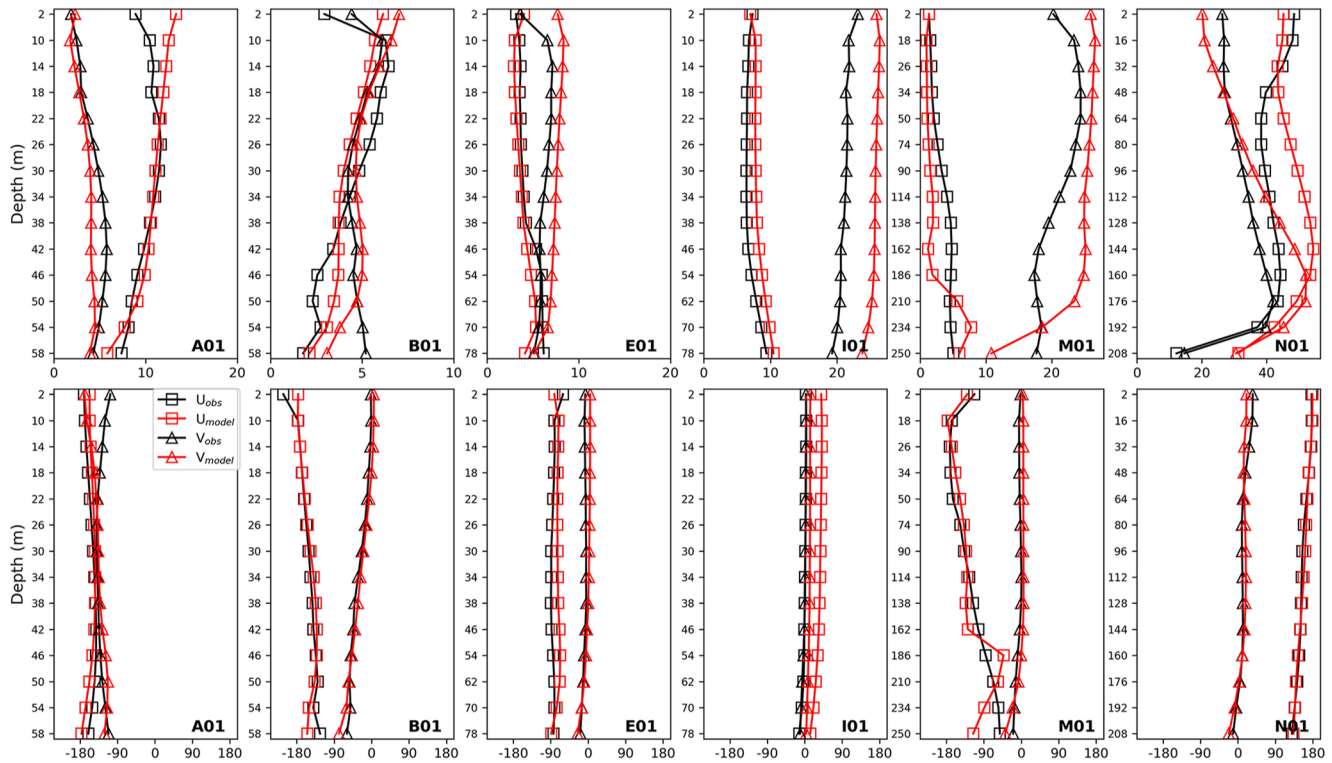


**Figure 2.** Comparison of vertical  $U$  &  $V$  velocities between the model and observations at 6 NERACOOS stations for M2 tidal velocity. The upper panels are the comparisons of M2 tidal velocity amplitudes (cm/s) and the lower panels are the corresponding comparisons of M2 tidal velocity phases (degree).

exist, especially for surface salinity at A01 and B01. Compared to other stations, I01 in the eastern GoME has a relatively small differences of temperature and salinity between the surface and bottom, and the model captures this characteristic well. M01 and N01 are deep stations with depths larger than 200 m. In the vertical, the salinity varies dramatically for these two stations. At station M01 (N01), the salinity increases from 32.6 (32.3) PSU in the surface to 34.5 (35.2) PSU in the bottom. For temperature, there is a clear three-layer structure with the colder Maine Intermediate Water trapped in the middle (Hopkins & Garfield, 1979; Townsend et al., 2006). The model successfully captures the general vertical structure observed at both N01 and M01.

Figures 3b and 3c show the Taylor diagrams for temperature and salinity, respectively. Overall, the model skill is higher for temperature than for salinity and higher at the nearshore stations (A01, B01, E01, I01) than at the offshore stations (M01, N01). In addition, the model skill generally decreases from the surface to the bottom. For the nearshore stations, the correlation coefficient ( $R$ ) for temperature is generally larger than 0.8, while  $R$  for salinity varies from around 0.3 to around 0.8. For the offshore stations,  $R$  for temperature is generally larger than 0.5 except for at two depths (150 and 180 m) of N01, while  $R$  for salinity is generally larger than 0.3 except for at two depths (1 and 180 m) of N01 and one depth (200 m) of M01. Furthermore, most of the normalized standard deviations and root mean square deviations are smaller than 1.0 or around 1.0, and larger deviations generally occur in the lower depths at offshore stations. Additional validation of the modeled temperature and salinity using shipboard CTD data is given in Figures S2 and S3 in Supporting Information S1 with higher model skills than these in Figure 3.

## 4. Results

### 4.1. GoME Salinity and Freshwater Fluxes From SS

Figure 4a shows freshwater inflow into the GoME across transect A1 and the mean salinity in the eastern and western GoME for 2017–2018. A correlation between freshwater flux across A1 and the mean salinity of the eastern GoME can be visually observed with an  $\sim 30$ -day lag of salinity to freshwater flux. The corresponding

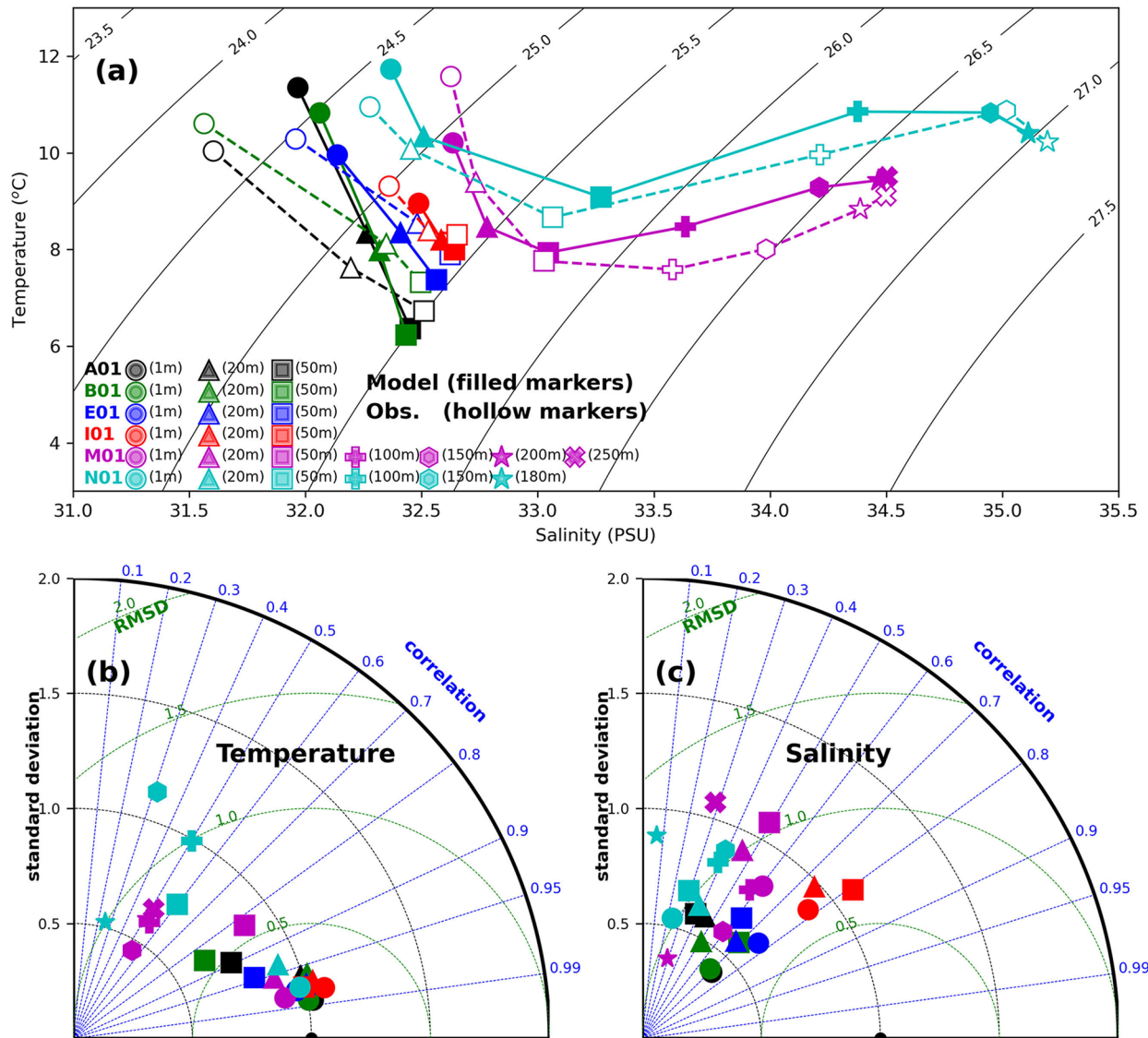


**Figure 3.** The upper panel (a) shows the comparison of temperature and salinity profiles between model and observations at six stations. The lower two panels are the Taylor Diagrams presenting the statistics for temperature (b) and salinity (c) at different depths and stations. Note both the standard deviation and root mean square deviation are normalized by the standard deviation of the corresponding observational data.

correction coefficient is  $-0.838$ ; the minus sign means that a larger freshwater flux is associated with lower salinity in the eastern GoME. However, there is no obvious correlation between the freshwater flux and the salinity in the western GoME, probably because the western GoME is farther downstream from the SS, and other factors such as local river runoff join to influence the salinity variation. The high correlation between the freshwater flux and mean salinity in the eastern GoME implies that the freshwater flux from SS is useful for studying the salt transport and budget in the GoME, consistent with the finding of Feng et al. (2016). In addition, we notice that salinity increased substantially in the eastern GoME during 2017–2018 and in the western GoME during 2018, which was observed at multiple locations inside GoME (Figure S4 in Supporting Information S1).

#### 4.2. Freshwater Fluxes Around SS and BB

Freshwater fluxes for the three transects (A2, A3, and B3, see Figure 1b for locations) enclosing SS during the period of 2017–2018 are shown in Figure 5a. For the freshwater flux through A3 ( $Q_{A3}^F$ ), there existed an obvious

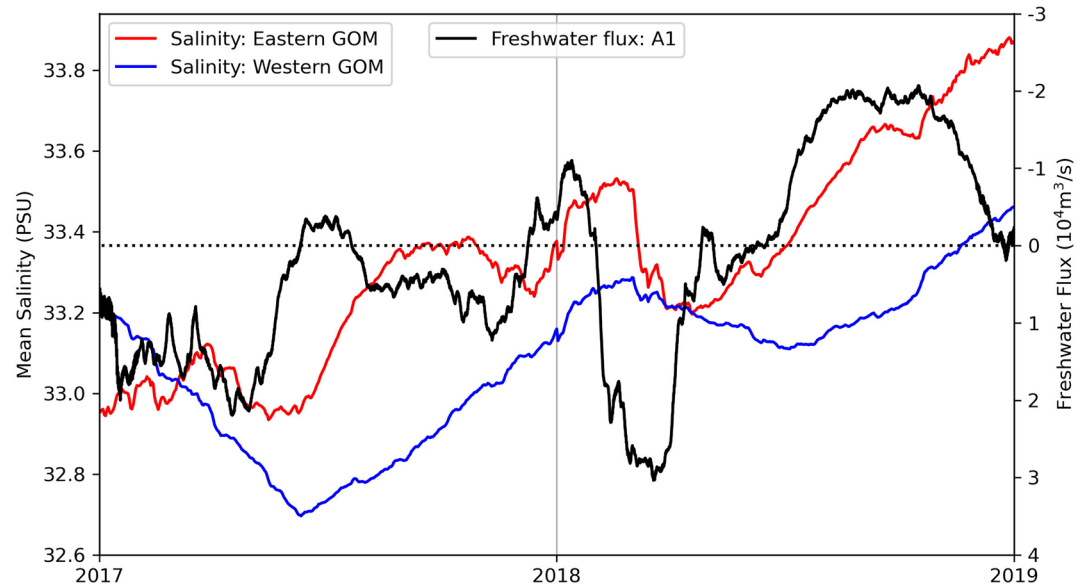


**Figure 4.** Time series of mean salinity in the eastern and western GoME, and freshwater flux across transect A1 (note the reversed y-axis).

seasonal cycle, maximum during winter and spring with the largest flux around  $1.0 \times 10^5 \text{ m}^3/\text{s}$ , and minimum during summer and fall when the flux can become negative at times. The seasonal cycle of freshwater flux through A2 ( $Q_{A2}^F$ ) generally followed  $Q_{A3}^F$  in 2017, but differed from  $Q_{A3}^F$  with the flux being particularly low in January and February 2018. The average  $Q_{A2}^F$  in 2017 was  $3.90 \times 10^4 \text{ m}^3/\text{s}$ . In contrast, the average  $Q_{A2}^F$  in 2018 was very low at only  $0.25 \times 10^4 \text{ m}^3/\text{s}$ . Furthermore,  $Q_{A2}^F$  in 2017 became negative only in June and July, while it almost remained negative from May to November in 2018. The significant positive  $Q_{A2}^F$  in March stood out in 2018 at about  $7.04 \times 10^4 \text{ m}^3/\text{s}$ . Compared to  $Q_{A2}^F$  and  $Q_{A3}^F$ , the freshwater flux through B3 ( $Q_{B3}^F$ ) did not show a clear seasonal cycle but varied strongly over 2017–2018 with multiple peaks.

Freshwater fluxes around BB are illustrated in Figure 5b.  $Q_{A2}^F$  represents the freshwater input from SS into the region around BB, while the freshwater flux through transect A1 ( $Q_{A1}^F$ ) represents the freshwater input from the SS to the GoME. The temporal pattern of  $Q_{A1}^F$  followed the variation of  $Q_{A2}^F$  but with a smaller magnitude, and  $Q_{A1}^F$  had a larger annual mean of  $0.74 \times 10^4 \text{ m}^3/\text{s}$  in 2017 compared to  $-0.31 \times 10^4 \text{ m}^3/\text{s}$  in 2018. The flux rate of  $Q_{A1}^F$  became negative in June and December of 2017. In contrast, negative flux rates were more prevalent in 2018 with positive fluxes only during the periods of February–April and June, which means that the general flow pattern through A1 in 2018 was completely different from that in 2017. Similar to  $Q_{A2}^F$ , the positive  $Q_{A1}^F$  in March stood out with a monthly mean flux rate of about  $4.80 \times 10^4 \text{ m}^3/\text{s}$ , the largest monthly flux rate through A1 during the entire period of 2017–2018. The freshwater flux through B1 ( $Q_{B1}^F$ ) was the major freshwater outflow of the BB region in 2017 with an average flux of about  $2.00 \times 10^4 \text{ m}^3/\text{s}$ . Overall, the change of flow patterns around BB caused similar variations of  $Q_{A1}^F$ ,  $Q_{A2}^F$ , and  $Q_{B1}^F$  from 2017 to 2018. The freshwater flux through B2 ( $Q_{B2}^F$ ), however, was different, dominated by positive values. In addition, the temporal variation of  $Q_{B2}^F$  was relatively small, representing a rather stable freshwater outflow across B2.

As shown in Figure 5b,  $Q_{A2}^F$  was generally balanced by the sum of  $Q_{A1}^F$ ,  $Q_{B1}^F$ , and  $Q_{B2}^F$ . This suggests the total freshwater was balanced instantaneously around BB, an enclosed region that is relatively small and shallow. Around SS, on the other hand, the sum of  $Q_{A2}^F$  and  $Q_{A3}^F$  did not exactly follow  $Q_{B3}^F$  (Figure 5a), although the patterns generally matched. This broad region has a much larger storage capacity of freshwater compared to the region around BB and the outflow lagged the inflow. Only a portion of the freshwater from SS was transported into the GoME through A1 in 2017, while the majority of it actually flowed out of the region through B1.  $Q_{B1}^F$  represents the FWT associated with the SSW that crosses the Northeast Channel and flows toward Georges Bank. Smith et al. (2001) found that there appeared to be a seasonal cycle to this crossover, stronger in winter. A similar conclusion was given by Shore et al. (2000) using drifter data and by Cho et al. (2002) through numerical modeling. The seasonal variation of  $Q_{B1}^F$  in 2017 was consistent with previous understanding, but the freshwater crossover

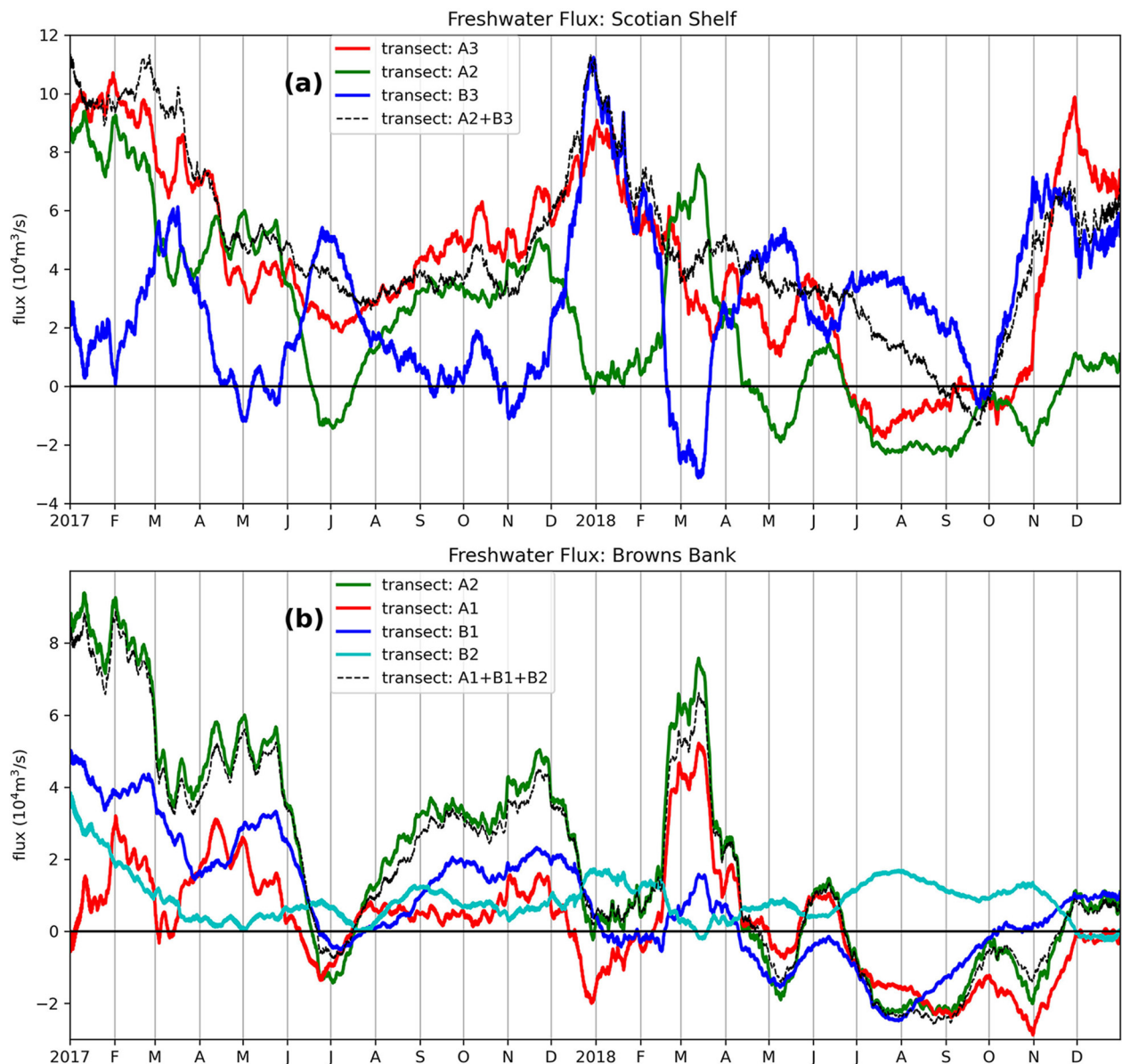


**Figure 5.** (a) Freshwater fluxes in 2017–2018 around SS for transects A3 (red), A2 (blue), and B3 (green), and (b) freshwater fluxes in 2017–2018 around Browns Bank for transects A2 (green), A1 (red), B1 (blue), and B2 (cyan). A 30-day running average was applied to all time series.

occurred frequently throughout the year. However, in 2018, the pattern of FWT in the SS and around BB was rather different. Most freshwater flowed from the continental shelf out into the ocean through transects B2 and B3. An exception occurred in March, when a large amount of freshwater entered the GoME through transect A1.

#### 4.3. Spatial Distribution of Freshwater

Freshwater thickness in the SS and GoME is presented in Figure 6. There was a large quantity of freshwater across much of the SS. More freshwater occurred in the eastern part of SS where freshwater thickness exceeded 12 m. Downstream, the freshwater region appeared to be squeezed toward the shore and its thickness decreased. In the SS, the freshwater spread more broadly seaward in 2018 than in 2017. However, inside the GoME, the pattern changed. In January 2017, a large quantity of freshwater entered the GoME (see also Figure 5b) and spread in the eastern GoME. By July 2017, the majority of freshwater was transported to the western GoME by the GoME Coastal Currents (Bisagni et al., 1996; Pettigrew et al., 1998, 2005). There was less freshwater entering

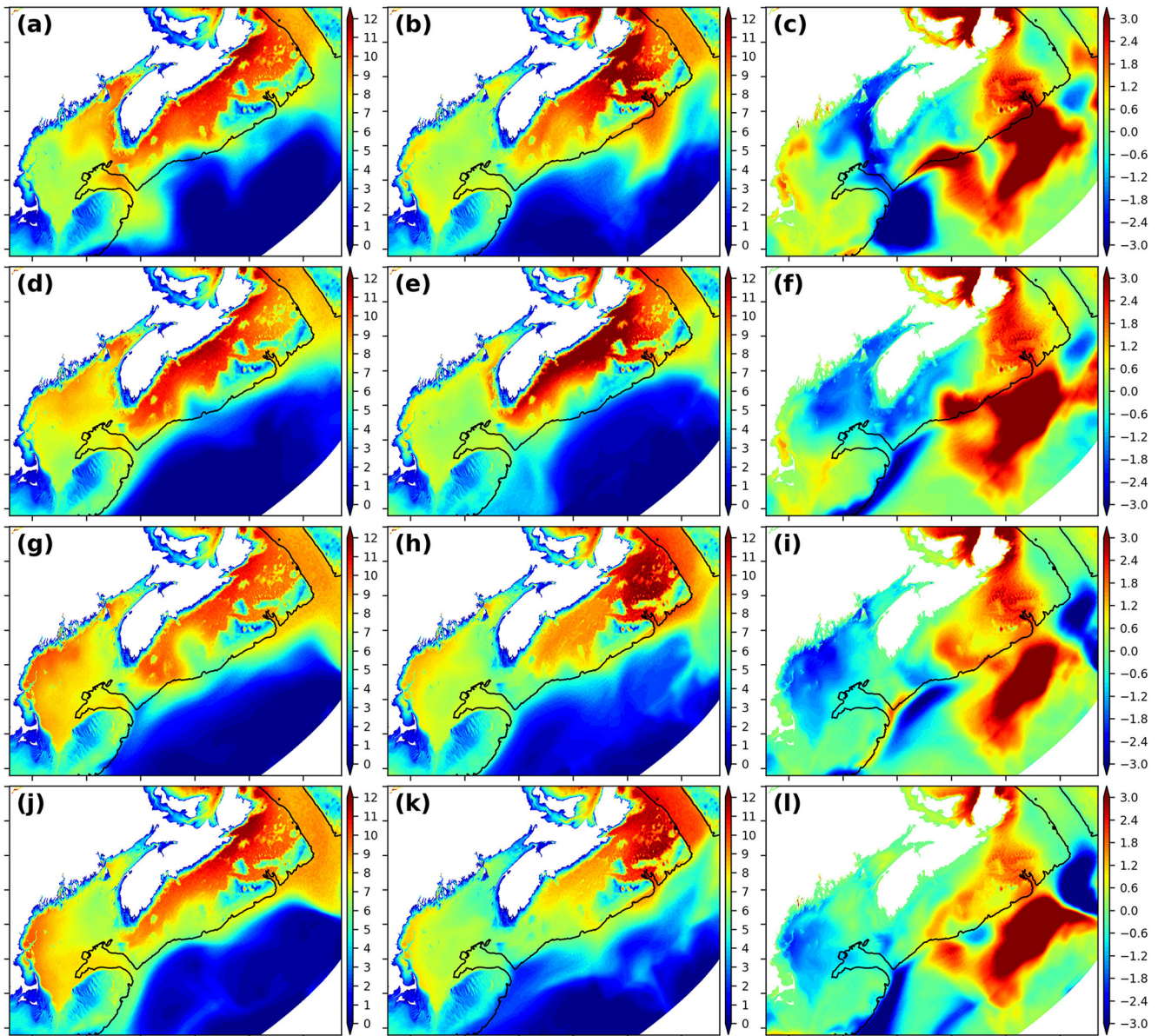


**Figure 6.** Spatial distribution of freshwater thickness (m) (see Equation 2) by integrating freshwater content in the top 100 m water column for January (a, b), March (d, e), July (g, h), and September (j, k). The left column is for 2017, the middle column is for 2018, and the right column is the difference between the two years ( $h_{2018}^F - h_{2017}^F$ ). The 200 m isobath (black line) is shown to indicate the location of shelf break.

the GoME through transect A1 in 2018 (see Figure 5b) and the freshwater thickness was thinner in the GoME compared to its counterpart in 2017. The only exception occurred in March 2018, when the freshwater thickness got thicker along the coast of Nova Scotia. In other months, negative  $Q_{A1}^F$  was frequent. As a result, the freshwater thickness in both the eastern and western GoME was much thinner in 2018, consistent with higher sea surface salinity in the GoME captured by satellite remote sensing (Grodky et al., 2018) and in situ observations (Figure S4 in Supporting Information S1). This also explains the patterns in Figure 4 showing the salinity in both the western GoME and the eastern GoME increased from 2017 to 2018.

### 5. Dynamics of FWT in the SS

Sections 4.2 and 4.3 show that the freshwater fluxes in the SS exhibit substantial variations. We further explore the drivers for FWT in the SS.

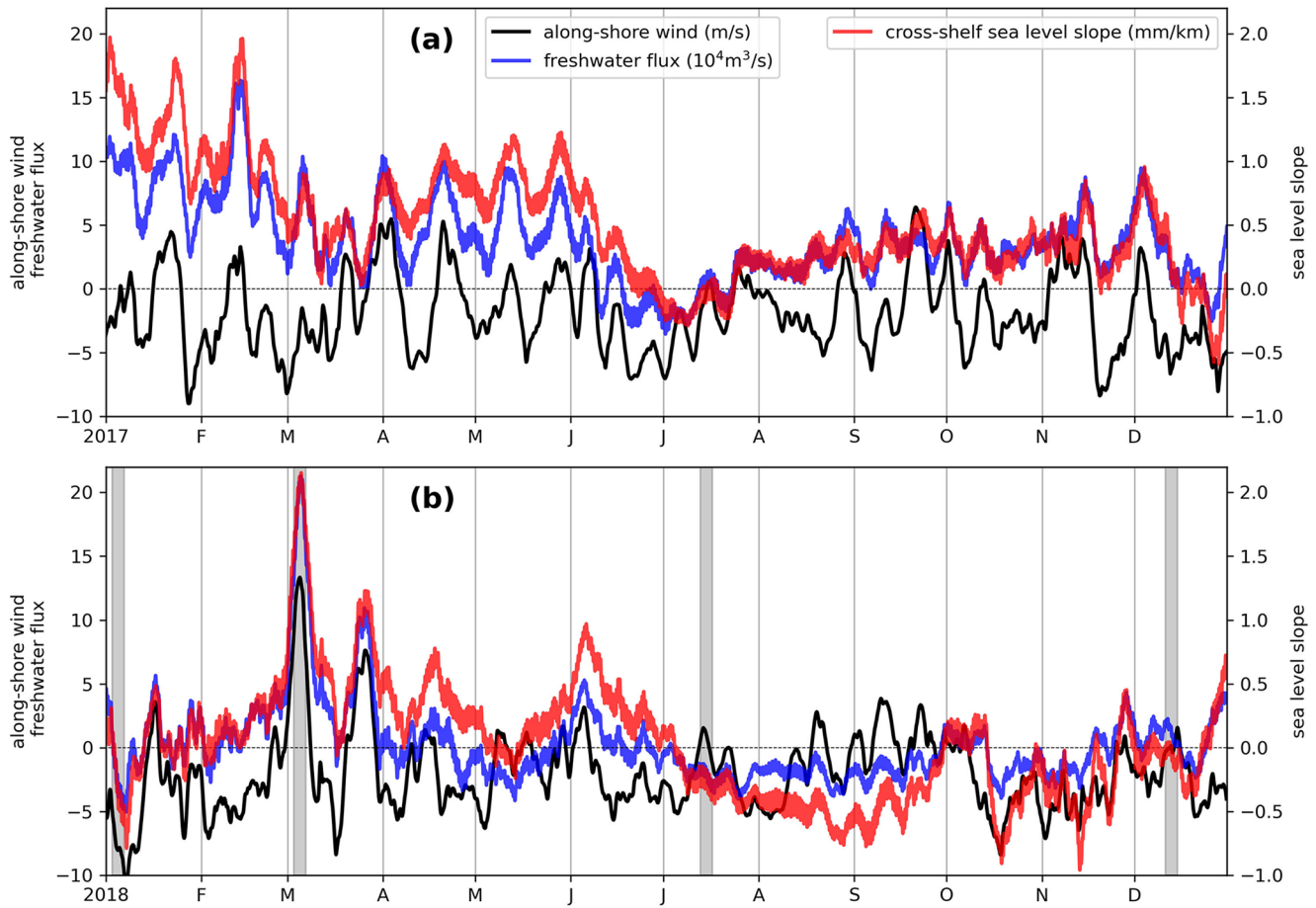


**Figure 7.** The upper panel (a) shows the 2017 time series of freshwater flux, cross-shelf sea level slope (positive value means higher elevation toward the coast) and along-shore wind component along transect A2 on the SS. Positive (negative) value of wind means that it blows southwestward (northeastward). A running average with a 5-day window is applied to all time series. The lower panel (b) shows the case in 2018. The shaded regions indicate the times when different forces of the momentum balance are evaluated throughout the SS in Figure 9.

### 5.1. The Prevailing Wind, Sea Level Slope, and FWT

Wind contributes significantly to the along-shelf momentum balance and plays an important role in the circulation and hydrography in the SS (Feng et al., 2016; Greenberg et al., 1997; Loder et al., 2003). The northeastward wind prevails over the SS, stronger in winter and weaker in summer (Hannah et al., 2001), which was more or less the case for 2017 and 2018 (Figure S5 in Supporting Information S1). Moreover, the NESS model shows that the sea surface elevation was higher at the northeastern end of SS than at the southwestern end for most of the time (Figure S6). This along-shelf slope was partially due to the alongshore wind stress that caused surface water to pile up on the eastern end of SS in combination with the baroclinic forcing as suggested by the freshwater thickness shown in Figure 6 (Csanady, 1981; Han et al., 1997). As a result, the elevation set-up at the northeastern end of SS provided a persistent driving force for the along-shelf southeastward flow.

### 5.2. Variability of Wind, Sea Level Slope, and FWT

The weakening and strengthening of alongshore wind also impact the sea surface elevation pattern in the SS hence the FWT. In Figure 7, the alongshore wind component (referred to as  $W_{\perp}$  hereafter), the corresponding cross-shelf elevation slope along A2 (referred to as  $\frac{\partial \eta}{\partial A2}$  hereafter), and the freshwater flux across A2,  $Q_{A2}^F$ , all filtered using a 5-day running mean to maintain the intraseasonal variability, are compared. The highest correlation was found between  $\frac{\partial \eta}{\partial A2}$  and  $Q_{A2}^F$  at 0.904. This strong correlation indicates a geostrophic balance in the cross-shelf direction (Csanady, 1981). Consistent with earlier studies (Noble & Butman, 1979; Sandstrom, 1980), there

existed some correlation between  $\frac{\partial \eta}{\partial A_2}$  and  $W_{\perp}$ . For example, the peaks and troughs of  $\frac{\partial \eta}{\partial A_2}$  roughly matched those of  $W_{\perp}$  during January–March, 2017 (Figure 7a). There also existed a higher correlation between  $Q_{A_2}^F$  and  $W_{\perp}$  with correlation coefficient of 0.499, validating the “valve” mechanism of Li et al. (2014) at weeks-to-months timescales. Overall, all these correlations are significant and they suggest that the responses to changing wind can be established rather quickly in the SS as most of wind events move across the SS within days (Sandstrom, 1980).

### 5.3. Southwestward Along-Shelf Wind and FWT

Although Li et al. (2014)’s “valve” mechanism can explain some variabilities of freshwater fluxes in the SS, there were also many mismatches between  $W_{\perp}$  and  $Q_{A_2}^F$  ( $\frac{\partial \eta}{\partial A_2}$ ) as shown in Figure 7. This suggests other factors modulating the flows. For example, the large (small)  $Q_{A_2}^F$  in 2017 (2018) cannot be explained by alongshore wind alone. Moreover, the relatively weak northeastward wind during August–September 2018 did not result in large positive freshwater fluxes in the SS. To further examine SS FWT in 2018, the surface elevation and normal velocities at the surface and 20 m at transect A2 and its extension are presented in Figure 8, while Figure S7 in Supporting Information S1 shows the counterparts in 2017.

The large  $Q_{A_2}^F$  of March 2018 (Section 4.2 and Figure 5b) was late because the large winter-spring flux was missing in January–February. The large  $Q_{A_2}^F$  in March can be attributed to two events of southwestward winds in early and late March (see both Figure 7b and Figure S5 in Supporting Information S1). These southwestward winds dragged the surface water southwestward as seen from Figure S8 in Supporting Information S1 when a general southwestward flow pattern dominated in March 2018 in the SS. The two southwestward wind events can be further identified in Figure 8 associated with two strong positive surface velocities (southwestward) during March 2018. Note that the influence of the southwestward wind almost disappeared at 20 m. Because freshwater tends to stay in the surface, these strong velocities resulted in the large freshwater fluxes in the SS with the timing matching that of strong southwestward winds (Figure 7b).

The causes of this strong increase of freshwater flux in March 2018 differ from the “valve” mechanism in two aspects. First, it was dominated by southwestward wind, while the “valve” mechanism is based on northeastward wind (Li et al., 2014). Second, the “valve” mechanism is based on a persistent sea level build-up on the eastern end of SS that provides a barotropic forcing for the entire water column. However, the increase of freshwater flux caused by these southwestward winds was a transient phenomenon manifested in the surface water. Figure 9b shows the different forces acting on the SS during the first southwestward wind event in March 2018. The large viscosity term arose from the strong wind forcing, and the large Coriolis term indicated the strong southwestward velocity. In general, in the cross-shelf direction, the Coriolis force was balanced by pressure gradient force (PGF) and viscosity. In the alongshore direction, the momentum balance is mainly achieved between the Coriolis force and the viscous forcing. The instantaneous response of surface velocity (Figure 8b) to the two wind impulses in March 2018 was accompanied by immediate surface-level perturbation (Figure 7b) in the cross-shore direction. However, the wind effect was limited to the surface layer as indicated by the diminishing response in the velocity at 20 m (Figure 8c). The rapid velocity reversal after the southwestward wind events suggests that the general balance in the alongshore direction below the surface was actually not disturbed, but was maintained by the long-term background alongshore PGF mentioned above.

### 5.4. Eddies and FWT

In early 2018, unlike the “valve” mechanism described by Li et al. (2014), the southwestward FWT remained relatively low even when the northeastward wind relaxed. The cause of this might be related to the warm-core ring near the western end of SS that started in October 2017 and persisted until February 2018 (Reul et al., 2020). This warm-core ring inhibited SSW from entering the GoME, a process indirectly supported by high salinity found in the eastern GoME (Figure 4) during January 2018 (Grotsky et al., 2018). On the other hand,  $Q_{B_3}^F$ , the freshwater outflow from the SS to the open ocean was high (see Figure 5a), suggesting that open ocean dynamic features can potentially impact the FWT on the SS. In Figure 8, multiple oceanic eddy events can be identified in 2018 that impinge on the SS. For example, in the beginning of 2018, an anticyclonic eddy was situated near the western end of SS 125–400 km from the coast (Figure 8 and Figure S8 in Supporting Information S1). The velocity along the extension of A2 was negative (flowing northeastward) 400–500 km from the coast. As time went on, the negative velocity zone moved toward SS until it reached the shelf break (about 125 km from the coast) in

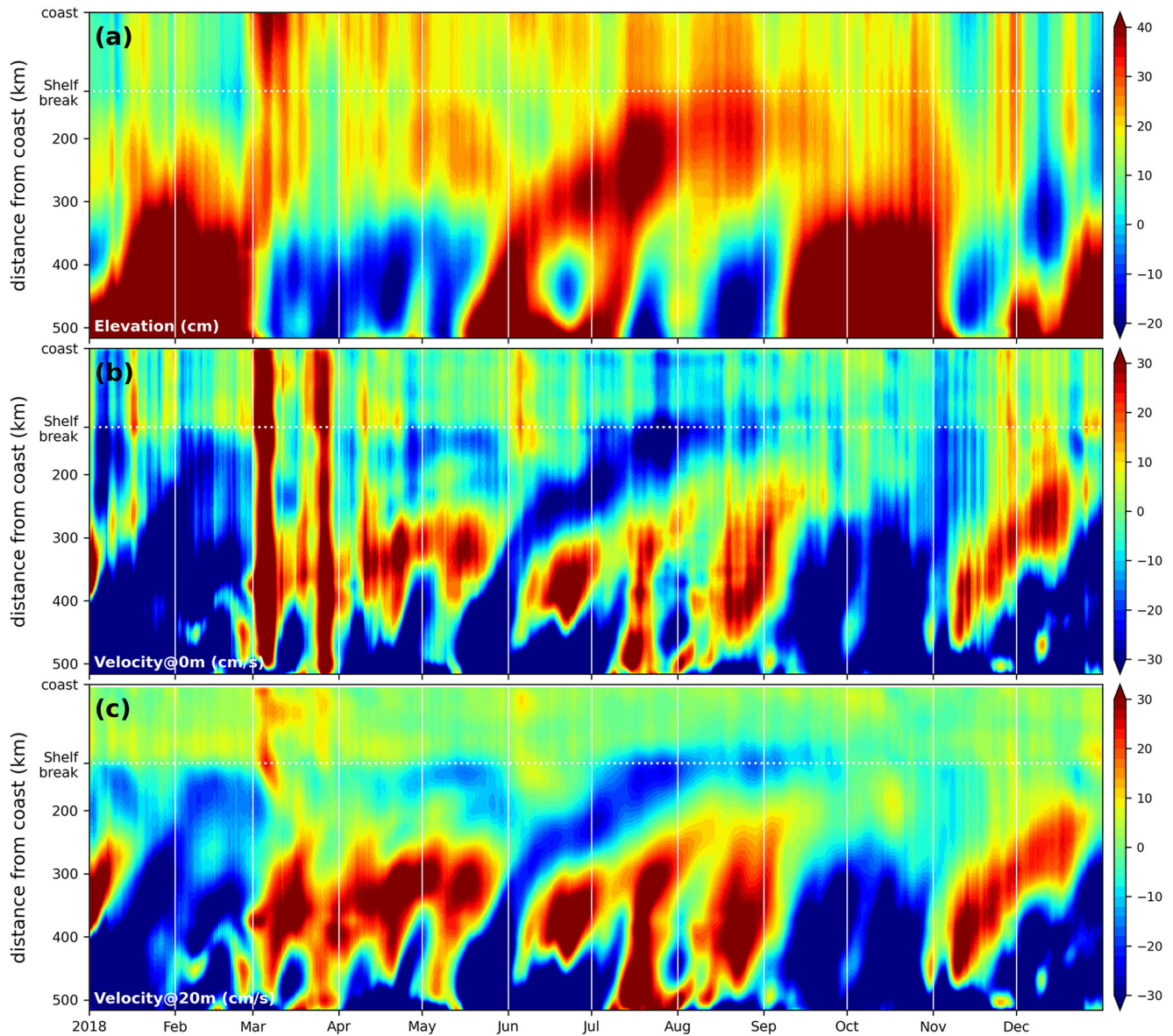


**Figure 8.** (a) The sea surface height (cm) along A2 (from the coast to the shelf break) and its extension to the domain boundary in 2018, the velocity components (cm/s) normal to transect A2 at the surface (b) and the 20 m depth (c), where the positive value represents water flows southwestward.

February. Figure 9a shows the momentum balance on January 5, 2018, exemplifying the cooccurrence of an anticyclonic eddy and strong eastward wind. The momentum balance was mostly maintained among Coriolis force, PGF and the viscosity term. The influence of an anticyclonic eddy on the SS can be inferred from the velocity, that is generally directed eastward with a larger magnitude in the offshore region than in the nearshore region. In addition, the PGF direction was generally northward, as an anticyclonic eddy has a larger surface height in its center. Therefore, the absence of large freshwater flux in early 2018 was likely due to the blockage of FWT by the anticyclonic eddy that appeared near the Northeast Channel during that time (Reul et al., 2020) in combination of the strong northeastward wind conditions. As the eddy faded in March, the along-shelf PGF was in favor of stronger FWT, which was another reason for the large  $Q_{A2}^F$  in March 2018 besides the southwestward wind events.

Figure 9c shows the momentum balance on July 15, 2018, another example of an anticyclonic eddy event but during a relaxation of northeastward wind. This anticyclonic eddy began in mid-May 2018 close to the NESS model boundary, and it impacted the shelf break and nearby BB from June through August (see Figure 8). The large northeastward velocity is clearly seen near the shelf break. In September, the eddy weakened at the surface,

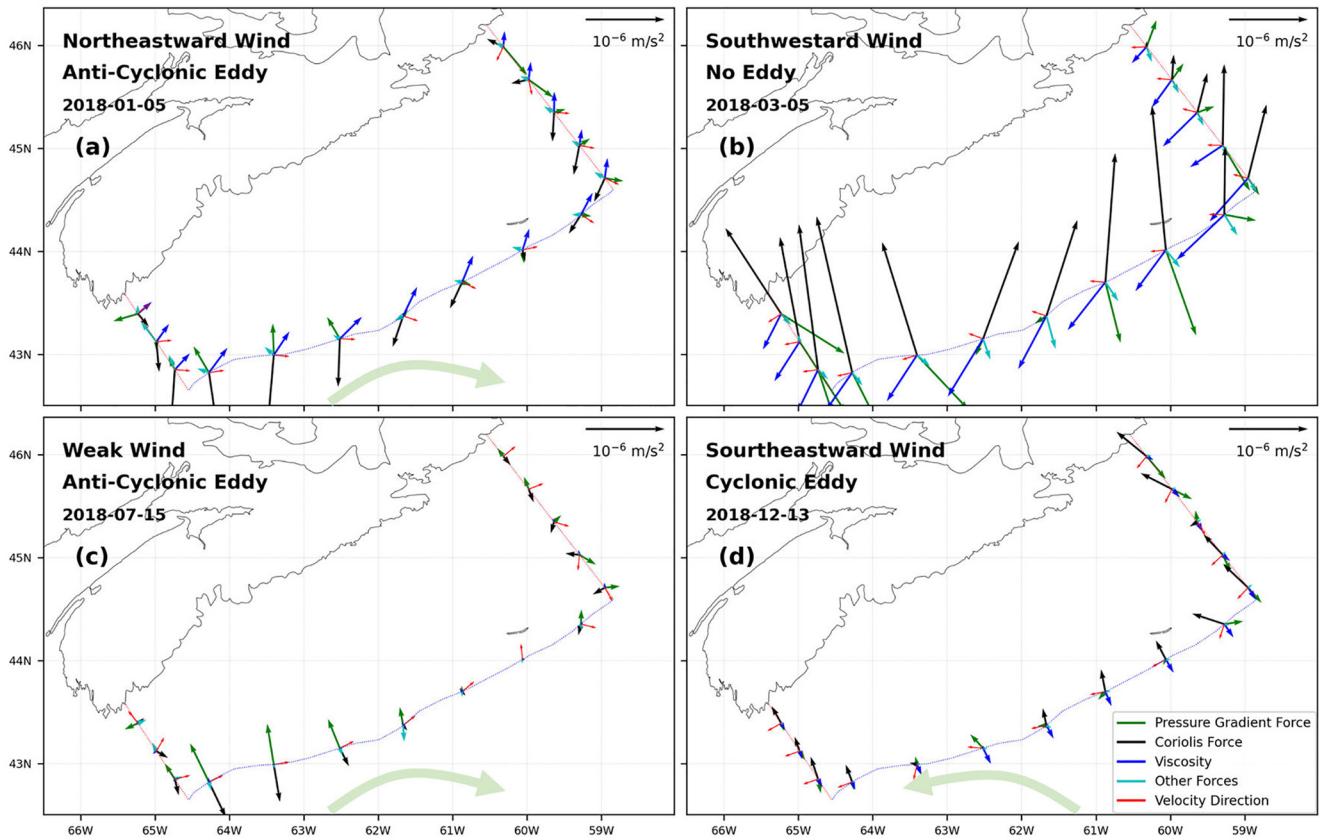


**Figure 9.** The momentum balance on SS along transects A2, A3, and B3 at 4 different times in 2018. The major forces of pressure gradient force (PGF), Coriolis force, and viscosity term are presented explicitly, while other forces (primarily advection) are shown combined. All Forces are depth-averaged in the upper 50-m water column. The left two panels present two scenarios in the presence of an anticyclonic eddy near the shelf break, with the former scenario (a) under strong eastward wind conditions and the latter one (c) under weak wind conditions. The upper right panel (b) shows the momentum balance during a strong southwestward wind. The lower right panel (d) shows a scenario in the presence of a cyclonic eddy near the shelf break, under eastward wind conditions. The velocity direction is indicated by the red arrow, while its strength is indicated by the length of Coriolis force term as Coriolis force is proportional to the velocity magnitude. In addition, the direction of eddies in the open ocean is indicated by the thick arrows.

but its signal was still visible at 20 m. Because the wind was weak, the viscosity term was negligible, and the PGF was directed to the north and was mainly balanced by the Coriolis force. Despite of weak eastward wind, the along-shelf PGF was weak in summer due to less freshwater supply from upstream. When an anticyclonic eddy impinged on the SS, it steered the flow on the shelf toward northeast. As a result,  $Q_{A2}^F$  decreased in July 2018 and remained low through September before the eddy (see Figures 5 and 7) completely dissipated in October.

In contrast, when a cyclonic eddy impinges on the continental shelf, it can potentially enhance the alongshore FWT by increasing southwestward velocities. In Figure 8c, we identified a cyclonic eddy event in November-December 2018. Although this eddy barely touched the shelf break, the southwestward velocity in the SS strengthened, resulting in an increasing trend of  $Q_{A2}^F$  even with the southeastward wind during the period. The corresponding momentum balance shown in Figure 9d suggests a primary balance among the Coriolis force, viscosity, and PGF. The influence of cyclonic eddies was more significant in 2017 (e.g., from July to November in Figure S7 in Supporting Information S1) resulting in high  $Q_{A2}^F$ . In contrast, anticyclonic eddies were more frequent in 2018 leading to generally lower FWT in the SS, which tended to block the transport of freshwater into the GoME (Figure 5) and most of the freshwater was retained in the SS as seen in Figure 6.

## 6. Summary

In this study, we constructed and validated a hydrodynamic model that covers the coastal seas around New England, and used it to investigate the spatiotemporal variations of the FWT on the SS in 2017–2018. Freshwater entered SS from the east at transect A3 and flowed out through the western end (transect A2) and the shelf break (transect B3), but there were large between-year variations: the annual mean of  $Q_{A3}^F$  in 2018 was only about half of that in 2017. Additionally, in 2017, freshwater flowed out through transect A2 was almost twice of the outflow through transect B3. In 2018, most of the freshwater flowed out through transect B3 with very limited outflow through transect A2.  $Q_{A2}^F$  even became negative in May 2018, which means that freshwater actually entered SS through transects A2 and A3, and flowed out through transect B3. In July 2018,  $Q_{A3}^F$  also became negative, presenting a different transport pattern with freshwater entering SS through transect A2 but exiting through A3 and B3.

There is a correlation between the salinity in GoME and the freshwater input from SS ( $Q_{A1}^F$ ). In the spring of 2017, large freshwater conveyed from the SS into the GoME led to the fresher eastern GoME. Along with the general cyclonic circulation inside the GoME, the freshwater was transported to the western GoME in the summer and fall. In contrast, the GoME salinity was significantly higher in 2018 due to the absence of freshwater input in the spring and generally smaller  $Q_{A1}^F$  in 2018, which was caused by more frequent anticyclonic eddies around the SS.

The momentum balance on SS was mainly achieved among Coriolis force, PGF, and the viscosity term (wind forcing). In the cross-shelf direction, the elevation slope is highly correlated with the FWT. In the along-shelf direction, the along-shore wind component dominated by northeastward wind plays an important role in setting up the FWT. However, we found that the southwestward wind events can dramatically increase the alongshore FWT. Furthermore, our analyses demonstrate that the FWT is also significantly influenced by oceanic eddies that impinge on the continental shelf: anticyclonic eddies tend to block the FWT, while cyclonic eddies can potentially increase the FWT. These findings enhance our understanding of FWT in the SS especially for synoptic to intraseasonal variability.

Note that the summary above was based on the two-year modeling results in 2017–2018, which may not be representative for the general dynamics in other years when other factors such as river fluxes and slope water inflow through the Northeast Channel play a dominant role over the SS current in the exchange between the GoME and its surrounding. The changes in the net of evaporation and precipitation (E-P) could also lead to variations in the salinity. Therefore, we computed E-P inside GoME during 2017–2018 (Figure S9 in Supporting Information S1), which is generally negative with an annual mean value of  $-595 \text{ m}^3/\text{s}$  in 2017 and  $-1,081 \text{ m}^3/\text{s}$  in 2018. The difference of  $Q_{A1}^F$  between 2017 and 2018 can be used to compare with that of E-P rate to infer their relative impacts on the salinity inside GoME, though the amount of  $Q_{A1}^F$  depends on the choice of reference salinity value. The  $Q_{A1}^F$  in 2018 is  $10,819 \text{ m}^3/\text{s}$  less than its counterpart in 2017, while E-P in 2018 is  $486 \text{ m}^3/\text{s}$  less than its counterpart in 2017. Given that the negative E-P is to make the GoME fresher and that the magnitude of the E-P change is much smaller than the change of  $Q_{A1}^F$  between the two years, E-P cannot be responsible for the higher salinity in GoME in 2018.

Lastly, SSW is not only less saline but also cold. In the SS, the heat fluxes generally follow the patterns of freshwater fluxes (Figure S10 in Supporting Information S1), which adds to the baroclinic forcing due to the freshwater flux to modulate the hydrodynamics locally. Furthermore, the temperature is an important factor for the stratification in the SS and GoME (Figure S2 in Supporting Information S1). Sinking of the Maine Surface Water inside GoME due to its coldness in winter and spring forms the Maine Intermediate Water, which results in the three-layer structure of water temperature (see Figure 3). However, the heat budget in GoME and SS is controlled by both the surface heat exchange with the atmosphere and the heat transport from SS and slope water, which needs further investigation for their relative contributions.

## Data Availability Statement

The model simulations are available at the University of Maine Dataverse Network (<http://dataverse.acg.maine.edu/dvn/faces/study/StudyPage.xhtml;jsessionid=38d38e5f51fafb5a3d174ec0d4c4?globalId=hdl:TEST/10301>), a cloud-based data repository.

## Acknowledgments

This study was supported by NASA grants NNX16AQ94A and NNX-16AG59G, and NSF grant OCE1458150 to the University of Maine. Numerical simulation was conducted on the computing system of Advanced Computing Group at the University of Maine. Some simulations used in this article were also conducted using the following computational facilities: (a) William & Mary Research Computing for providing computational resources and/or technical support (URL: <https://www.wm.edu/it/rc>); (b) the Extreme Science and Engineering Discovery Environment (XSEDE; Grant TG-OCE130032), which is supported by National Science Foundation grant number OCI-1053575; (c) Texas Advanced Computing Center (TACC), The University of Texas at Austin for providing HPC resources that have contributed to the research results reported within this article. The authors acknowledge the use of the following datasets in this study for model set-up and validation: (a) bathymetry data from US Coastal Relief Model (<https://www.ngdc.noaa.gov/mgg/coastal/crm.html>) and General Bathymetric Chart of the Oceans (<https://www.gebco.net/>); (b) boundary forcing from FES2014 tide database (<https://datastore.csls.fr/catalogues/fes2014-tide-model/>) and HYCOM reanalysis (<https://www.hycom.org/>); (c) atmospheric forcing from the North American Regional Reanalysis database (<http://www.emc.ncep.noaa.gov/mmb/rreanal/>); (d) streamflow data from USGS (<https://waterdata.usgs.gov/nwis>); (e) observed water level from National Ocean Service NOAA (<https://tidesandcurrents.noaa.gov/>) and Fisheries and Oceans Canada (<http://www.isdm-gdsi.gc.ca/isdm-gdsi/twl-mne/index-eng.htm>); (f) buoy data from NERACOOS (<http://www.neracoos.org/datatools>), and CTD data from World Ocean Database (<https://www.ncei.noaa.gov/products/world-ocean-database>).

## References

- Bigelow, H. B. (1927). *Physical oceanography of the Gulf of Maine*. US Government Printing Office.
- Bisagni, J., Beardsley, R., Ruhsam, C., Manning, J., & Williams, W. (1996). Historical and recent evidence of Scotian Shelf Water on southern Georges Bank. *Deep Sea Research Part II: Topical Studies in Oceanography*, 43(7–8), 1439–1471. [https://doi.org/10.1016/S0967-0645\(96\)00041-0](https://doi.org/10.1016/S0967-0645(96)00041-0)
- Brown, W., & Irish, J. (1993). The annual variation of water mass structure in the Gulf of Maine: 1986–1987. *Journal of Marine Research*, 51(1), 53–107. <https://doi.org/10.1357/002224093223828>
- Cho, Y. K., Beardsley, R. C., & Sheremet, V. A. (2002). On the cause of Scotian Shelf Water crossovers. *Geophysical Research Letters*, 29(24), 65–16564. <https://doi.org/10.1029/2002gl014968>
- Csanady, G. T. (1981). Circulation in the coastal ocean. *Advances in Geophysics*, 23, 101–183. [https://doi.org/10.1016/S0065-2687\(08\)60331-3](https://doi.org/10.1016/S0065-2687(08)60331-3)
- Drinkwater, K., Mountain, D., & Herman, A. (1998). Recent changes in the hydrography of the Scotian Shelf and Gulf of Maine—A return to conditions of the 1960 s? *Sci. Coun. Res. Doc. NAFO*, 98, 16.
- Drinkwater, K., Petrie, B., & Smith, P. (2002). *Hydrographic variability on the Scotian Shelf during the 1990s*.
- Feng, H., Vandemark, D., & Wilkin, J. (2016). Gulf of Maine salinity variation and its correlation with upstream Scotian Shelf currents at seasonal and interannual time scales. *Journal of Geophysical Research: Oceans*, 121(12), 8585–8607. <https://doi.org/10.1002/2016jc012337>
- Greenberg, D. A. (1979). A numerical model investigation of tidal phenomena in the Bay of Fundy and Gulf of Maine. *Marine Geodesy*, 2(2), 161–187. <https://doi.org/10.1080/15210607909379345>
- Greenberg, D. A., Loder, J. W., Shen, Y., Lynch, D. R., & Naimie, C. E. (1997). Spatial and temporal structure of the barotropic response of the Scotian Shelf and Gulf of Maine to surface wind stress: A model-based study. *Journal of Geophysical Research: Oceans*, 102(C9), 20897–20915. <https://doi.org/10.1029/97jc00442>
- Grodsky, S. A., Vandemark, D., Feng, H., & Levin, J. (2018). Satellite detection of an unusual intrusion of salty slope water into a marginal sea: Using SMAP to monitor Gulf of Maine inflows. *Remote Sensing of Environment*, 217, 550–561. <https://doi.org/10.1016/j.rse.2018.09.004>
- Han, G., Hannah, C. G., Loder, J. W., & Smith, P. C. (1997). Seasonal variation of the three-dimensional mean circulation over the Scotian Shelf. *Journal of Geophysical Research: Oceans*, 102(C1), 1011–1025. <https://doi.org/10.1029/96jc03285>
- Hannah, C. G., Shore, J. A., Loder, J. W., & Naimie, C. E. (2001). Seasonal circulation on the western and central Scotian Shelf. *Journal of Physical Oceanography*, 31(2), 591–615. [https://doi.org/10.1175/1520-0485\(2001\)031<0591:scotwa>2.0.co;2](https://doi.org/10.1175/1520-0485(2001)031<0591:scotwa>2.0.co;2)
- Hopkins, T., & Garfield, N., III. (1979). Gulf of Maine intermediate water. *Journal of Marine Research*, 37(1), 103–109.
- Inceze, L., Xue, H., Wolff, N., Xu, D., Wilson, C., Steneck, R., et al. (2010). Connectivity of lobster (*Homarus americanus*) populations in the coastal Gulf of Maine: Part II. Coupled biophysical dynamics. *Fisheries Oceanography*, 19(1), 1–20. <https://doi.org/10.1111/j.1365-2419.2009.00522.x>
- Ji, R., Davis, C. S., Chen, C., Townsend, D. W., Mountain, D. G., & Beardsley, R. C. (2007). Influence of ocean freshening on shelf phytoplankton dynamics. *Geophysical Research Letters*, 34(24). <https://doi.org/10.1029/2007gl032010>
- Ji, R., Davis, C. S., Chen, C., Townsend, D. W., Mountain, D. G., & Beardsley, R. C. (2008). Modeling the influence of low-salinity water inflow on winter-spring phytoplankton dynamics in the Nova Scotian Shelf-Gulf of Maine region. *Journal of Plankton Research*, 30(12), 1399–1416. <https://doi.org/10.1093/plankt/fbn091>
- Li, D., Wang, Z., Xue, H., Thomas, A., & Philip, Y. (2021). Seasonal variations and driving factors of the Eastern Maine Coastal Current. *Journal of Geophysical Research: Oceans*, 126. <https://doi.org/10.1029/2021jc017665>
- Li, Y., Ji, R., Fratantoni, P. S., Chen, C., Hare, J. A., Davis, C. S., & Beardsley, R. C. (2014). Wind-induced interannual variability of sea level slope, along-shelf flow, and surface salinity on the Northwest Atlantic shelf. *Journal of Geophysical Research: Oceans*, 119(4), 2462–2479. <https://doi.org/10.1002/2013jc009385>
- Loder, J. W. (1998). The coastal ocean off northeastern North America: A large-scale view. *The Sea*, 11, 105–138.
- Loder, J. W., Hannah, C. G., Petrie, B. D., & Gonzalez, E. A. (2003). Hydrographic and transport variability on the Halifax section. *Journal of Geophysical Research: Oceans*, 108(C11). <https://doi.org/10.1029/2001jc001167>
- Moriarty, P., Byron, C., Pershing, A., Stockwell, J., & Xue, H. (2016). Predicting migratory paths of post-smolt Atlantic salmon (*Salmo salar*). *Marine Biology*, 163(4), 74. <https://doi.org/10.1007/s00227-016-2847-5>
- Noble, M., & Butman, B. (1979). Low-frequency wind-induced sea level oscillations along the east coast of North America. *Journal of Geophysical Research: Oceans*, 84(C6), 3227–3236. <https://doi.org/10.1029/jc084ic06p03227>
- Pettigrew, N. R., Churchill, J. H., Janzen, C. D., Mangum, L. J., Signell, R. P., Thomas, A. C., et al. (2005). The kinematic and hydrographic structure of the Gulf of Maine Coastal Current. *Deep Sea Research Part II: Topical Studies in Oceanography*, 52(19–21), 2369–2391. <https://doi.org/10.1016/j.dsr2.2005.06.033>
- Pettigrew, N. R., Townsend, D. W., Xue, H., Wallinga, J. P., Brickley, P. J., & Hetland, R. D. (1998). Observations of the Eastern Maine Coastal Current and its offshore extensions in 1994. *Journal of Geophysical Research: Oceans*, 103(C13), 30623–30639. <https://doi.org/10.1029/98jc01625>
- Ramp, S. R., Schlitz, R. J., & Wright, W. R. (1985). The deep flow through the Northeast Channel, Gulf of Maine. *Journal of Physical Oceanography*, 15(12), 1790–1808. [https://doi.org/10.1175/1520-0485\(1985\)015<1790:tdftn>2.0.co;2](https://doi.org/10.1175/1520-0485(1985)015<1790:tdftn>2.0.co;2)
- Reilly, J. E., Evans-Zetlin, C., & Busch, D. A. (1987). Primary production. In R. H. Backus (Ed.), *1987 Georges Bank* (pp. 220–233). Cambridge, Mass: MIT Press.
- Reul, N., Grodsky, S., Arias, M., Boutin, J., Catany, R., Chapron, B., et al. (2020). Sea surface salinity estimates from spaceborne L-band radiometers: An overview of the first decade of observation (2010–2019). *Remote Sensing of Environment*, 242, 111769. <https://doi.org/10.1016/j.rse.2020.111769>
- Sandstrom, H. (1980). On the wind-induced sea level changes on the Scotian shelf. *Journal of Geophysical Research: Oceans*, 85(C1), 461–468. <https://doi.org/10.1029/jc085ic01p00461>
- Shore, J. A., Hannah, C. G., & Loder, J. W. (2000). Drift pathways on the western Scotian Shelf and its environs. *Canadian Journal of Fisheries and Aquatic Sciences*, 57(12), 2488–2505. <https://doi.org/10.1139/f00-214>
- Smith, P. C. (1983). The mean and seasonal circulation off southwest Nova Scotia. *Journal of Physical Oceanography*, 13(6), 1034–1054. [https://doi.org/10.1175/1520-0485\(1983\)013<1034:tmasco>2.0.co;2](https://doi.org/10.1175/1520-0485(1983)013<1034:tmasco>2.0.co;2)
- Smith, P. C., Houghton, R. W., Fairbanks, R. G., & Mountain, D. G. (2001). Interannual variability of boundary fluxes and water mass properties in the Gulf of Maine and on Georges Bank: 1993–1997. *Deep Sea Research Part II: Topical Studies in Oceanography*, 48(1–3), 37–70. [https://doi.org/10.1016/S0967-0645\(00\)00081-3](https://doi.org/10.1016/S0967-0645(00)00081-3)
- Smith, P. C., Pettigrew, N. R., Yeats, P., Townsend, D. W., & Han, G. (2012). Regime shift in the Gulf of Maine. *American Fisheries Society Symposium*, 79, 185–203.

- Townsend, D. W., Pettigrew, N. R., Thomas, M. A., Neary, M. G., McGillicuddy, D. J., Jr, & O'Donnell, J. (2015). Water masses and nutrient sources to the Gulf of Maine. *Journal of Marine Research*, 73(3–4), 93–122. <https://doi.org/10.1357/002224015815848811>
- Townsend, D. W., Thomas, A. C., Mayer, L. M., Thomas, M. A., & Quinlan, J. A. (2006). Oceanography of the northwest Atlantic continental shelf (I, W). *The Sea*, 14, 119–168.
- Umlauf, L., & Burchard, H. (2003). A generic length-scale equation for geophysical turbulence models. *Journal of Marine Research*, 61(2), 235–265. <https://doi.org/10.1357/002224003322005087>
- Xue, H., Chai, F., & Pettigrew, N. R. (2000). A model study of the seasonal circulation in the Gulf of Maine. *Journal of Physical Oceanography*, 30(5), 1111–1135. [https://doi.org/10.1175/1520-0485\(2000\)030<1111:amsots>2.0.co;2](https://doi.org/10.1175/1520-0485(2000)030<1111:amsots>2.0.co;2)
- Zhang, Y., Ateljevich, E., Yu, H. C., Wu, C. H., & Yu, J. C. S. (2015). A new vertical coordinate system for a 3D unstructured-grid model. *Ocean Modelling*, 85, 16–31. <https://doi.org/10.1016/j.ocemod.2014.10.003>
- Zhang, Y., Ye, F., Stanev, E. V., & Grashorn, S. (2016). Seamless cross-scale modeling with SCHISM. *Ocean Modelling*, 102, 64–81. <https://doi.org/10.1016/j.ocemod.2016.05.002>